This is a post-referee draft, the final version is available at

https://doi.org/10.1016/j.jeurceramsoc.2023.02.005

Crack Healing Mechanisms in Atmospheric Plasma Sprayed Yb-Silicate Coatings during Post-Process Heat Treatment

Emine Bakan[a]*, Robert Vaßen[a]

[a] Forschungszentrum Jülich GmbH, Institute of Energy and Climate Research, Materials Synthesis and Processing (IEK-1), 52425 Jülich, Germany

*Corresponding Author. Forschungszentrum Jülich GmbH, Institute of Energy and Climate Research, Materials Synthesis and Processing (IEK-1), 52425 Jülich, Germany, Tel: +49 2461 61 2785; Fax: +49 2461 61 2455, e-mail: e.bakan@fz-juelich.de.

Abstract

The microstructural evolution of partially amorphous, atmospheric plasma-sprayed Yb-silicate coatings was investigated after heat treatment (HT, 1300 °C). Open porosity as well as crack area and widths in the coatings were characterized. A correlation was found between the increasing amorphous content of the as-sprayed coatings and the reduction in crack area due to crack healing after HT. Characterization results also suggested larger crack widths in the coatings after HT. The first crack-healing mechanism proposed was the capillarity-driven viscous flow of the amorphous phase in the coatings. It was experimentally shown that viscous flow-driven crack spheroidization (crack width enlargement), and crack healing started in the coatings at 1050 °C. Secondly, metastable to stable phase transformation (> 1100 °C) induced expansion in the constrained coatings was discussed as a crack healing mechanism. Finally, a two-step heat treatment was designed to prevent crack width enlargement during HT resulting in reduced porosity.

Keywords: Environmental barrier coating, atmospheric plasma spray, crystallization, crack healing, porosity

1. Introduction

SiC fiber reinforced/SiC matrix ceramic matrix composite (SiC/SiC CMC) material system offers both high temperature and structural capability for the next generation of gas turbine engines. Together with their low density, SiC/SiC CMC enables reductions in cooling air need, engine weight, fuel burn, and harmful exhaust emissions in gas turbine engines [1-4]. Si-based materials form a silica (SiO_2) scale by oxidation (O_2, H_2O) at elevated temperatures however in the engine atmosphere silica reacts to water vapor to form a volatile secondary product (e.g. $Si(OH)_4$). While the scale grows according to a parabolic rate law, it volatilizes according to a linear rate which gives rise to paralinear kinetics [5]. In laboratory tests, the volatility was found to be accelerating with the increased temperature according to an Arrhenius relationship, as well as with increased pressure (P) and gas velocity (v) ($P^{3/2} v^{1/2}$ for laminar flow) [6]. Engine tests also confirmed the high rates of SiC loss in the gas turbine combustion environment [7]. These results implied the requirement of protective coatings to shield the silica-forming components from combustion and other high-temperature environments containing H_2 or H_2O during long-term use. For this purpose, Environmental Barrier Coatings (EBCs) are being developed since mid of the 90s [8-23].

Currently, a typical EBC system consists of a Si bond coat for oxidation protection and improved adhesion, and a volatilization barrier topcoat made of rare earth silicates such as $Yb_2Si_2O_7$. Although this two-layer structure resembles a well-established thermal barrier coating system (TBCs), the topcoat in EBCs is required to be dense (ideally gas-tight) unlike in TBCs. This difference brought one of the main challenges in EBC manufacturing using conventional deposition methods such as atmospheric plasma spraying (APS) and electron beam physical vapor deposition (EB-PVD) as micro or macro-cracked (e.g. lamellar, segmented microstructures) coatings deposited by APS or columnar-type coatings produced by EB-PVD cannot fulfill the gas tightness requirement for the EBC topcoat. Furthermore, glass-forming silicates tend to form amorphous coatings when deposited with the established manufacturing techniques at typical deposition temperatures of 300-500 °C. Highly crystalline and dense silicate coatings without typical interlamellar or intrasplat porosity could be achieved by plasma spraying into a box furnace where the substrate is held at ~1200 °C [19]. Similarly, heating the substrate with the plasma plume prior to and after the deposition to reach deposition temperatures above 1000 °C was shown to be an effective way to increase crystallinity and minimize porosity for lab-scale samples [21]. However, the feasibility of these modified spray processes remains questionable for industrial coating manufacturing. Therefore a more common approach has been a post-process heat treatment to induce crystallization in the amorphous silicate deposits manufactured by conventional deposition processes. In the literature, various post-heat treatment programs were reported either as a single-step heat treatment at high temperature or multiple-step heat treatment at different temperatures and durations (Table 1). That said, the microstructural changes in the constrained coatings after the heat treatments were rarely reported. Table 1 summarizes the porosity levels (sum of open and close porosity) published in a few studies before and after the applied heat treatments, which suggests an increasing trend compared to the as-sprayed condition. Depending on whether or not the porosity is interconnected after the heat treatment, this increase would be undesirable in terms of permeability of oxidants through the coating thickness.

Table 1: Literature summary of heat treatment procedures and porosity levels of conventionally APS deposited coatings from $Yb_2Si_2O_7$ feedstock.

Heat treatment (HT)	Porosity % (as-sprayed)	Porosity % (after HT)	Porosity measurement method	Reference
1200 °C – 2 h	-	-	-	[24]
700 °C – 2 h 960 °C – 2 h 1033 °C – 20 h 1200 °C – 20 h 1300 °C – 4 h	2-14	-	Archimedes	[25]
1300 °C – 4 h	5.3	-	Image analysis	[26]
1300 °C – 4 h	3.18	5.95	3D X-ray microtomography	[27]
1300 °C – 100 h	4-7	5.5-6	Image analysis	[28]
1200 °C – 2 h	2.4	-	Image analysis from free-standing coating	[29]
1300 °C – 20 h	1.9-3	3-4.5	Image analysis	[30]

Therefore, the objective of the study reported here was to improve the understanding of the microstructural evolution in conventionally APS-sprayed Yb-silicate coatings during post-process treatment. To that end, the porosity volume and size of three different APS Yb-silicate coatings deposited at various spray currents were analyzed before and after heat exposure using mercury intrusion porosimetry and image analysis methods. Crystallization shrinkage and thermal expansion of the as-sprayed coatings were measured by dilatometry. The sintering behavior of amorphous Yb-silicate particles as well as coatings was investigated at various temperatures chosen based on the dilatometric findings. Hypotheses for crack healing mechanisms were proposed and tested. Finally, using the gained understanding, a two-step heat treatment procedure was developed which enabled reducing the total porosity and crack widths in the plasma sprayed Yb-silicate coating after the crystallization heat treatment.

2. Materials and Method

2.1 Coating deposition and characterization

The Yb-silicate coatings were manufactured by using a commercial $Yb_2Si_2O_7$ feedstock (15-65 µm, Oerlikon Metco US Inc., Westbury, New York, USA) in a MultiCoat system (Oerlikon Metco, Wohlen, Switzerland) with a three-cathode TriplexPro 210 spray torch mounted on a six-axis robot (IRB 2400, ABB, Switzerland). The plasma gas composition was 49 Ar/1 H_2 standard liter per minute, the spray current was varied (275/325/375 A), the robot velocity was 500 mm/s and the stand-off distance was 90 mm. Metallographic cross-sections of the coatings were prepared for microstructural investigations via scanning electron microscopy (SEM, TM-4000, Hitachi, Tokyo, Japan).

2.2 Dilatometry

Dilatometry measurements of APS Yb-silicate coatings were performed between room temperature and 1400 °C in air with a Netzsch DIL 402C dilatometer (Netzsch GmbH, Selb, Germany) using a heating rate of 10 K/min. ~2 mm thick Yb-silicate coatings at each spray current mentioned in section 2.1 were deposited on graphite substrates and subsequently, the substrates were mechanically removed to obtain free-standing coatings. Half part of the free-standing coatings was heat treated in a box furnace (1300 °C – 20h) and after that, the as-sprayed and heat-treated coatings were machined into 3x2x25 mm^3 bars for dilatometry measurements.

2.3 Mercury Intrusion Porosimetry

The open volume and pore size distribution of the coatings were determined by mercury intrusion porosimetry (MIP) according to ISO 15901-1 standard (Belpore HP, Microtrac Retsch GmbH, Haan, Germany). Using the spray conditions described in section 2.1, Yb-silicate coatings were deposited with a thickness of ~600 µm on Si bond coated (APS process parameters are described elsewhere [31]) porous SiC substrates (HalSiC-R, Morgan Advanced Materials, Waldkraiburg, Germany) as described in Fig 1. Two samples were prepared at each spray current used for Yb-silicate deposition, one of the samples was analyzed in the as-sprayed state and the second one was heat-treated in a box furnace at 1300 °C – 20 h in air using a heating rate of 10 K/min. Following this, the Si bond-coated porous SiC substrates were mechanically ground to achieve free-standing Yb-silicate coatings in the as-sprayed and annealed state. For the mechanical grinding, the coated sides of the samples were glued on metallic supports using a thermoplastic polymer (Crystalbond 509**,** Cloeren Technology GmbH, Wegberg, Germany). A metallographic diamond grinding wheel (DIPLAS P200, Cloeren Technology GmbH, Wegberg, Germany) was used for the grinding process, and after the grinding, the glue was dissolved in methyl ethyl ketone (T-E-Klebetechnik, Hannover, Germany) overnight and then in an ultrasonic bath for 2 h. The top surface of the coating (glued part) was also ground about 50 µm to prevent any contribution of roughness in MIP measurements. After the grinding, the final average roughness (R_a) of the both sides of the free-standing coatings were ~1 µm.

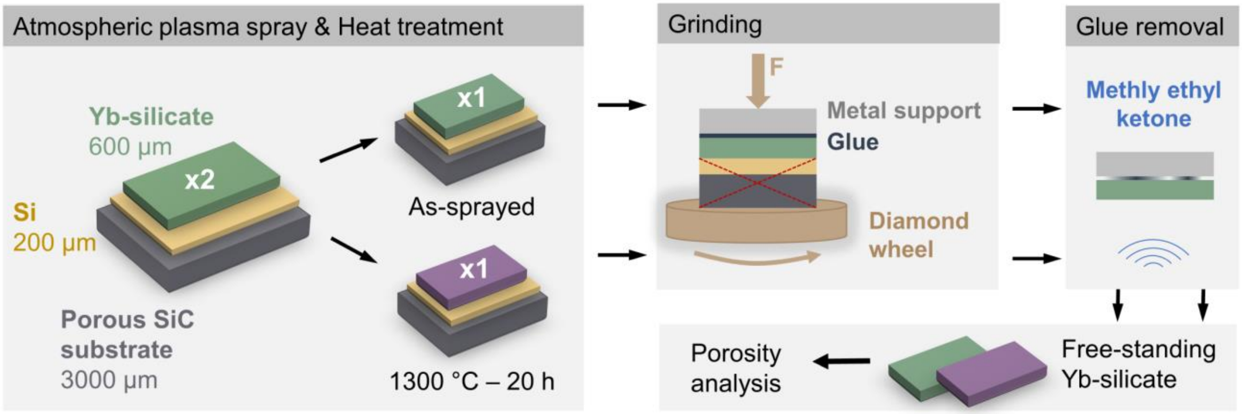

Figure 1: Sample preparation steps for mercury intrusion porosimetry analysis.

2.4 Image processing and analysis

Back-scattered scanning electron microscope (BSE-SEM, TM-4000, Hitachi, Tokyo, Japan) images (0.1 µm/pixels) were processed and analyzed using ImageJ software (open source) to quantify the changes in the crack width and crack area of the Yb-silicate coatings before and after the post-process heat treatment. The image processing steps are shown in Fig.2. In the first step, the SEM images (1) were converted to binary images (1b). In the second step, by using circularity and size filters as well as the watershed algorithm for segmentation, the crack network was isolated from the remaining porosity such as pores stemming from imperfect filling or unmolten particles (1c). After that, binary skeleton images (1d, gray value 0 for the background, and gray value 1 for pixels on the line) and distance maps (1e) were produced from crack network images (1c). The distance map shows for every pixel inside the crack the distance to its outer contour and this distance has its maximum in the middle of the crack which is equivalent to half crack width. The skeleton images mark the middle line of the crack with a single-pixel width. Therefore multiplication of 1d and 1e selects the pixels along the middle line of cracks in distance maps, which have gray values equal to the maximum distance in other words half-width of cracks. The last image on the right in Fig. 2 shows the result after using Fire Lookup Table (LUT) to convert the grayscale image to a colored one. In order to quantify the crack widths from half crack width maps, the histogram data of these maps which includes pixel counts and the gray values were used. The mean crack width per SEM image was calculated according to:

$$\text{Mean crack width (pixels)} = 2 \times \frac{\sum(\text{gray values x pixel counts})}{\sum \text{pixel counts (gray value} > 0)} \quad (1)$$

and converted to µm using the µm/pixels scale of the image. The crack area per SEM image was determined using crack network images (1c).

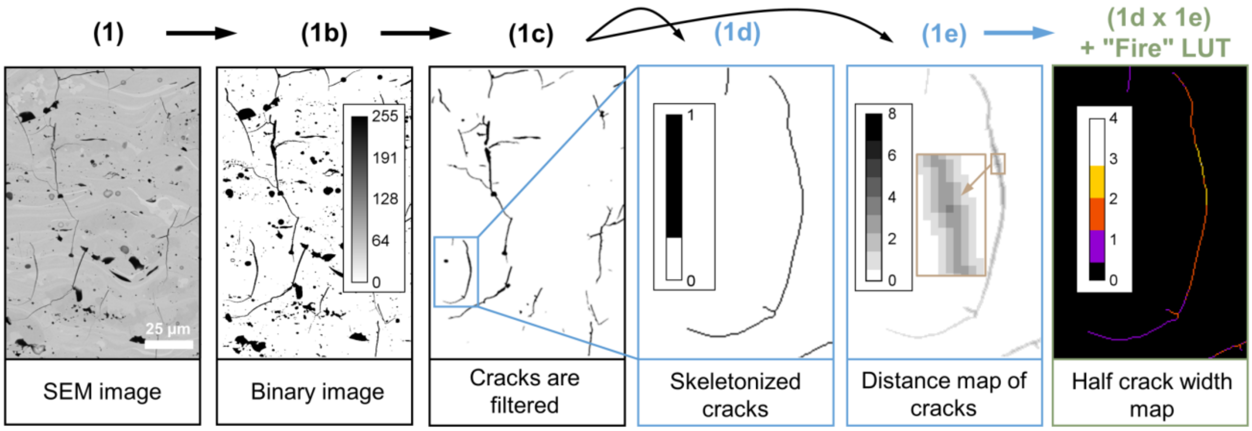

Figure 2: Image processing steps for crack width measurements. The SEM image belongs to the as-sprayed Yb-silicate coating deposited at 275 A. The scales of the images show the gray value of the pixels in each image.

2.5 Manufacturing of glass Yb-silicate particles and sintering experiment

For sintering experiments, glass Yb-silicate particles were manufactured by atmospheric plasma spraying the $Yb_2Si_2O_7$ feedstock (see details in 2.1) into distilled water with no robot movement. The spray conditions were the same as that of the coatings except for the spray current (425 A) and the stand-off distance (~ 500 mm). After spraying, the water was drained and the quenched particles were dried in air at 70 °C overnight. Following that 5 grams of loose quenched powder were sintered in zirconia crucibles at various temperatures between 950-1300 °C for 10 h in a box furnace. Metallographic cross-sections of the sintered pellets or powder were prepared for microstructural SEM investigations.

3. Results and Discussion

3.1 Microstructure of coatings

The microstructure of APS Yb-silicate coatings sprayed at 275, 325, and 375 A can be seen in Fig. 3 in the as-sprayed state and after the heat treatment (1300 °C – 20 h). Higher spray current leads to greater heat and momentum transfer to the particles [32] as well as increased substrate temperatures resulting in more complete melting of the particles, flattening of the molten droplets upon impact and consequently a denser microstructure. In agreement with that, less partially molten particles were observed at higher spray currents (Fig. 3a-c). Furthermore, X-ray diffraction (XRD) analysis results which are not shown here for the sake of brevity were consistent with these results. According to XRD analyses, each coating was highly amorphous in the as-sprayed state, amorphous content slightly increased at higher spray currents as well as the secondary Yb_2SiO_5 content (9, 14, and 23 wt.% at 275, 325, and 375 A, respectively, after the heat treatment) as a result of higher particle temperatures. The reader is referred to [21, 28, 31, 33-35] for more details on the processing, amorphous content, and phase composition relations of Yb-silicate coatings.

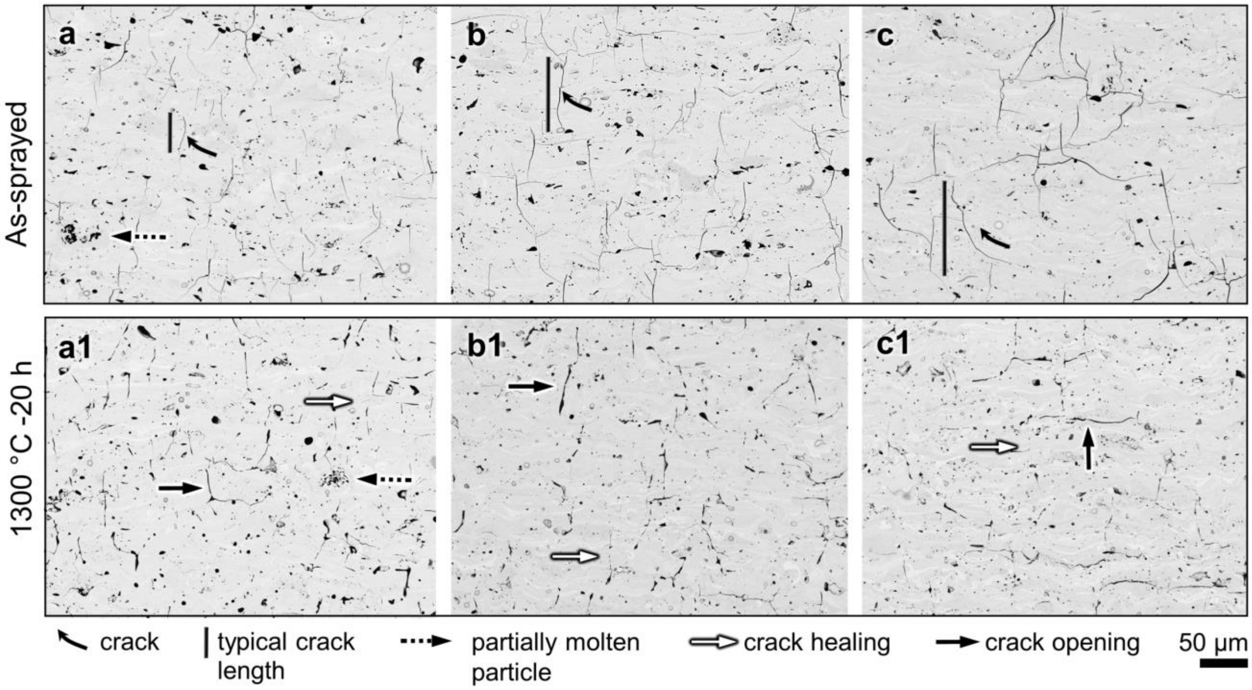

Figure 3: Cross-section microstructure of Yb-silicate coatings deposited at 275 A (a, a1), 325 A (b, b1), and 375 A (c, c1) in the as-sprayed state (a, b, c) and after heat treatment (a1, b1, c1). Note that the heat treatment of the coatings was performed on the substrates.

Along with the densification in the microstructures at the higher spray currents, changes in the microcrack patterns were observed, i.e. microcracks were arrested in the single lamella (deposition pass) at the coldest spray condition (Fig. 3a) while they propagated through two or more lamellae at the hotter spray conditions (Fig. 3 b-c). The microcracks originate from the relaxation of quenching (always tensile) and thermal stresses (depends on CTE, tensile during cooling if $\alpha_{coating}>\alpha_{substrate}$) in APS deposited coatings [36]. Quenching stresses in the splats ($\sigma_q = \alpha_c \times E_0 \times (T_m - T_s), \alpha_c$=CTE of the deposit, E_0=bulk elastic modulus, T_m= melting point, T_s=substrate or deposition temperature) evolve during deposition and result from rapid solidification and cooling down to deposition temperature afterward. As the thermal contraction is constrained by the underlying substrate or deposit, in-plane tensile quenching stress is developed within the splats. Individual stress state in every single splat contributes to the macroscopic quenching stresses of the coating together with the pore volume in the microstructure. A positive correlation between the deposition temperatures and measured quenching stresses in the ceramic APS coatings was found and associated with the improved bonding between splats which increases the elastic modulus of the deposit and possibly lessens the stress relaxation via interfacial sliding [36-38]. These relations, which were mainly established for zirconia or alumina coatings deposited on metallic substrates, are even more complex for APS Yb-silicate coatings due to their amorphous content and the presence of the secondary phase in these coatings with different physical and mechanical properties. For instance, the bulk elastic modulus of Yb_2SiO_5, the amount of which increases at hot spray conditions, was reported lower than that of $Yb_2Si_2O_7$ (132 GPa vs. 168 GPa) [39] while the CTE of Yb_2SiO_5 was measured larger than that of $Yb_2Si_2O_7$ (7.5 ppm/K vs. 4.1 ppm/K) [33]. Table 2 shows the calculated bulk elastic moduli of the coatings deposited at different spray currents by taking into account the volume fractions of the phases. Quenching stresses in the single splat scale estimated from these bulk elastic moduli as well as measured CTE of the coatings (after heat treatment, see section 3.2) indicated an increasing trend towards high spray currents. In the macroscopic scale, due to higher porosity at the cold spray condition, a more significant reduction in elastic modulus can be expected with respect to the hot spray condition meaning a more effective reduction of quenching stresses in the former. Based on these simplified estimations it can be speculated that the relaxation of higher quenching stresses at the hotter spray conditions could be the reason for the propagation of the microcracks through well-bonded lamellae akin to the formation of segmentation cracks [40-42]. However note that these estimations ignore the increasing amorphous contents in the coatings from colder towards hotter spray conditions and hence the resultant changes in the temperature-dependent material properties as well as relevant stress relaxation mechanisms for glassy phases. Finally, tensile thermal stresses were estimated in the coatings (30-70 MPa, Table 2) using the bulk moduli, which could also contribute to the larger crack widths measured at the hotter spray conditions (see further discussion in section 3.4).

Table 2: Estimated quenching stress in the APS Yb-silicate splats using bulk elastic moduli. Note that thermal stress was also estimated using bulk elastic moduli.

Spray current (A)	$Yb_2Si_2O_7$ volume fraction in the coating	Coating (bulk) elastic modulus (GPa)	CTE of coating (ppm/K)	Deposition temperature (°C)	Quenching stress (GPa)	Thermal stress (MPa)
275	0.92	165	5.4	400	1.19	31
325	0.87	163	5.6	500	1.28	54
375	0.79	160	5.7	600	1.33	74

After the heat treatment, there were significant changes in the coating microstructures in terms of porosity (Fig. 3 a1-c1). Crack healing was observed in each microstructure while the cracks which were not healed in the heat treatment were observed to be more open after the heat treatment in comparison with the as-sprayed state. The quantitative changes in the crack area, crack width, and total porosity of the coatings after the heat treatment will be presented in section 3.4.

3.2 Dilatometry measurements

Fig.4 shows the dilatometry measurement results of APS Yb-silicate coatings in the as-sprayed state and after heat treatment (1300 °C – 20 h). In the as-sprayed state, each coating showed a rapid shrinkage at ~1050 °C and then an expansion at ~1200 °C, similar to the reported results in [25]. The shrinkage was attributed to the crystallization process while the expansion was shown to be a result of metastable ($Yb_2Si_2O_7$ (P-1), Yb_2SiO_5 ($P2_1/c$) and $Yb_{4.67}Si_3O_{13}$ ($P6_3/m$)) to stable ($Yb_2Si_2O_7$ ($C2/m$), Yb_2SiO_5 ($I2/a$)) phase transformation in a recent work [43]. Based on these findings, the greater degree of shrinkage and expansion measured at higher spray currents in this work can be associated with higher amorphous content and hence larger volume of metastable phases at hotter spray conditions.

As mentioned above, Yb_2SiO_5 content in the $Yb_2Si_2O_7$ coatings was higher at hotter spray conditions due to more pronounced SiO_2 evaporation. This could be indirectly confirmed by dilatometry measurements performed after heat treatment (Fig.4). As the coatings were fully crystalline after the heat treatment, linear expansions were measured in each coating which yielded slightly larger CTE (Fig.4) at higher spray currents presumably due to the higher volume of Yb_2SiO_5 phase.

Based on the dilatometry measurement results in the as-sprayed state, the implication was that the shrinkage and expansion in the constrained Yb-silicate coatings would induce tensile and compressive stresses, respectively. Tensile stresses may result in new porosity and cracks in the microstructure while compressive stress could be helpful for further densification via crack healing as observed in Fig. 3 a1-c1. The effect of crystallization and metastable phase transformation on microstructure will be further discussed together with the temperature-dependent heat treatment results of the coatings in section 3.6.

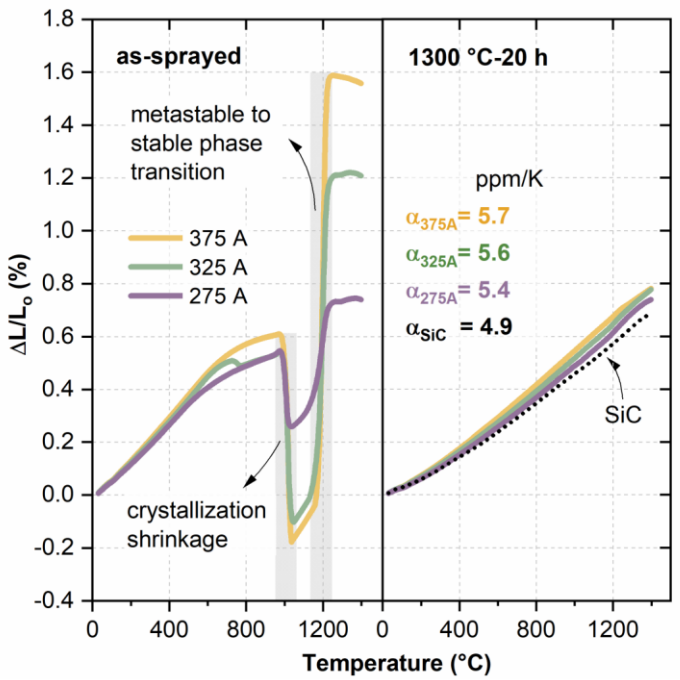

Figure 4: Dilatometry measurements results of Yb-silicate coatings sprayed at 275/325/375 A between room temperature and 1400 °C, in the sprayed state and after heat treatment (1300 °C-20 h).

3.3 Mercury Intrusion Porosimetry

In the mercury intrusion porosimetry (MIP) method, the pore volume is measured by the volume of the mercury intruded into open pores under applied pressure while pore diameters are calculated assuming a cylindrical pore geometry according to the Washburn equation ($d_{pore} = 4\gamma cos\theta/p$, r_{pore}= pore diameter (diameter of cylinder), γ=surface tension of mercury, θ=wetting angle, p=pressure) [44]. The cumulative open porosity (%) in the Yb-silicate coatings sprayed at 275/325/375 A as a function of calculated pore diameters is shown in Fig.5. In the as-sprayed state, the cumulative porosity of the coatings decreased from 5.5 % to 3.3 % with the increase in spray current from 275 A to 375 A. After the heat treatment, there was a systematic increase (~1 %) in the cumulative porosity of the coatings, however, this increase was particularly questionable at 325 and 375 A as in some of these samples very large pores (50-100 µm diameter, equivalent to ~1/10 to 1/5 of total coating thickness) were detected. Such porosity was found only in the as-sprayed state at 325 A and only after the heat treatment at 375 A. This discrepancy between the measurement results of the same coatings before and after the heat treatment implied that these pores could be measurement artifacts. The volume of the very large pores was close to 1 % in each case and it should be noted that 1 % is a typical standard error for the MIP porosity measurements of plasma sprayed coatings. Consequently, it was not clear whether there was a total porosity increase of 1 or 2 % at 325 A after the heat treatment or whether was there any increase at all at 375 A.

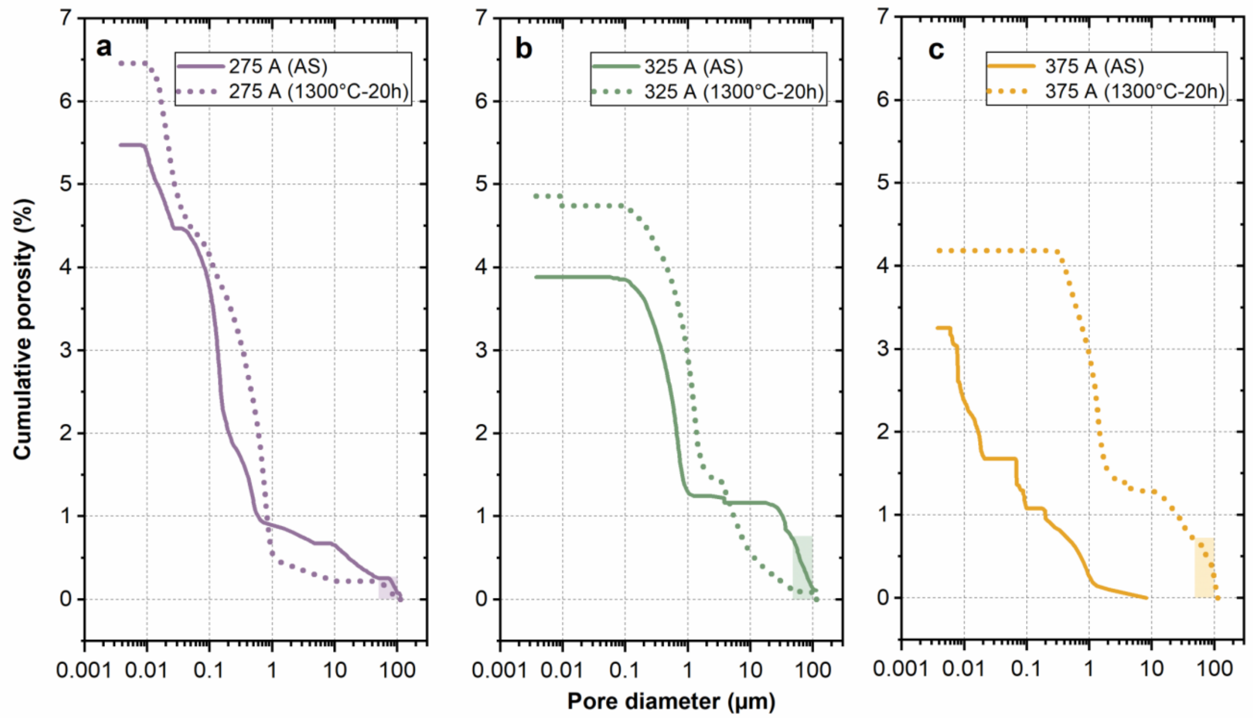

Figure 5: Mercury intrusion porosimetry results of Yb-Silicate coatings sprayed at 275 A (a), 325 A (b), and 375 A (c) spray current in the sprayed state and after heat treatment (1300 °C – 20 h). The shaded parts at the bottom end of the curves mark the presence of very large pores (50-100 µm) and their volume which were detected in some of the samples.

Another systematic change observed in the MIP measurement results was the increase in the pore sizes after the heat treatment. In typical bimodal MIP curves of APS coatings, the part of the curve where the cumulative pore volume constantly increases at the pore diameters of ~0.5-1 µm is correlated with the interlamellar cracks in the microstructure [45-47]. The smaller pore sizes than these can be associated with the intrasplat cracks and unmelted particles, and the larger ones with globular pores. Based on that, the consistent shift of the MIP curves (<1 µm) to the larger pore diameters after the heat treatment was attributed to the enlarged crack openings as observed in Fig. 3. Furthermore, pore coarsening due to the sintering phenomenon could be a contributing factor to the shift of MIP curves to the larger diameters [48]. Nevertheless, due to the necessity of shape factors to convert cylindrical pore diameters to the pore size of different pore shapes (e.g cracks) in the coating microstructure, it was not possible to quantify the changes in the crack widths from MIP measurements reliably. Therefore image analysis was used for this purpose and the results will be discussed in the following section.

3.4. Image analysis results and crack healing hypotheses

The crack area and crack widths of the Yb-silicate coatings determined by the image analysis in the as-sprayed state (AS) and after the heat treatment (HT, 1300 °C – 20 h) are shown in Fig. 6a-b. Firstly, the crack area distribution was found to be notably wider at 375 A than at the other two spray currents. This could be attributed to changing crack density per SEM image at this spray current, i.e. one SEM image at the selected magnification was largely free of cracks, while another image was full of cracks at this spray current. This was not the case at colder spray conditions as the crack lengths were smaller and the cracks were more homogenously distributed through thickness resulting in similar crack density in each SEM image.

Comparison of the mean crack areas (or median as the values were approximately close almost in all cases) in the as-sprayed and heat-treated state of the Yb-silicate revealed dependency on the spray current. At 275 A and 325 A the changes in the mean crack areas were minimal after the heat treatment, if any, it was slightly larger after the heat treatment at 275 A while it was a little lower at 325 A. The drop in the mean crack area was more pronounced at 375 A after the heat treatment. At all spray currents, the mean crack width was increased after the heat treatment in agreement with the MIP results. Both in the as-sprayed state and after the heat treatment, the mean crack widths were getting larger from colder towards hotter conditions.

The lower mean crack area at 325 A and 375 A after the heat treatment (Fig. 6a) despite increased mean crack widths (Fig. 6b) indicated reduced crack lengths in the coatings which can be attributed to the crack healing process. As the mean crack area was lower at 375 A after the heat treatment in comparison with the 325 A while the mean crack widths were larger, a more effective crack healing at 375 A could be concluded. Although the crack healing also took place at 275 A according to Fig. 3a1, the mean crack area did not change significantly in this coating after the heat treatment, if any it slightly increased, (Fig 6a) suggesting that the crack length reduction could not overcome the crack width enlargement during the healing process.

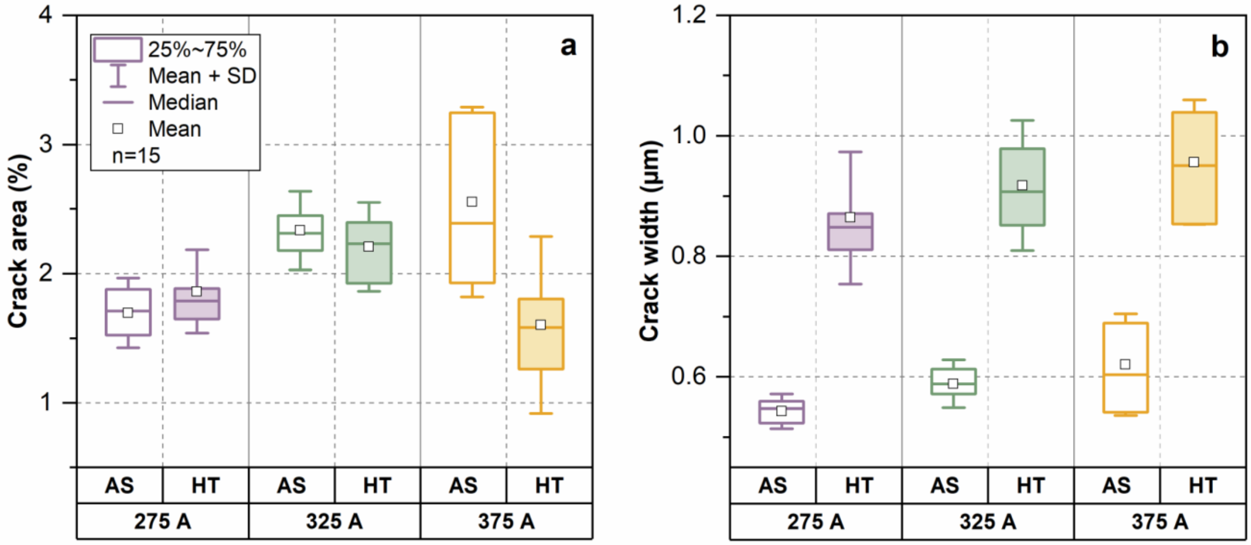

Figure 6: Crack area (%) (a) and crack width (b) of APS Yb-silicate coatings determined by the image analysis in the as-sprayed state (AS) and after the heat treatment (HT, 1300 °C – 20 h).

Thermal crack healing in glasses is described by the capillarity-driven viscous flow of the glass [49-51]. In this process, when the glass is heated above the glass transition temperature, the viscosity drops and due to viscous flow driven by capillary forces, the sharp crack tips get rounder, and crack widths enlarge. In other words, provided that the viscosity is low enough, cracks transform into spheres to reduce the surface energy, and then the spherical cavity is filled by the glass which completes the crack healing process. On the contrary, if the initial viscosity is too high around the cracks e.g. if crystallinity is higher, viscous flow driven by capillary forces is impeded. In that case, crack healing relies on the thermally activated diffusion process which requires annealing at high temperatures (e.g. > 0.7 T_m ~ >1300 °C for Yb-silicates) for long periods.

Therefore densification rate in glasses that are prone to crystallization during heating is highly dependent on whether crystallization occurs before a high degree of densification via viscous flow is achieved or not. According to the literature, the formation of more than 10-15 vol. % of crystals prior to the final stage of glass sintering can seriously limit the ability to reach high density [52, 53].

Based on these, the first hypothesis to explain crack healing (~crack area reduction) in APS Yb-silicate coatings was the viscous flow of the amorphous phase during heating to annealing temperature (1300 °C). Higher amorphous content in the coatings sprayed at hotter conditions could explain the more effective crack healing in these coatings. Furthermore, spheroidization of the cracks during this process could explain the crack width enlargement during the heat treatment (Fig. 6b). Secondly, the residual stresses in the coatings could play a role in crack healing or opening. In the as-sprayed state, the larger thermal stresses (tensile) in the coatings sprayed under hotter conditions (Table 2) may be responsible for the larger crack widths (Fig. 6b). In the heating phase of the heat treatment, firstly a stress relaxation in Yb-silicate coating can be assumed via the viscous flow. Following that crystallization shrinkage would induce tensile stresses in the constrained coating and finally M→S transformation could lead to compressive stresses as the coating cannot freely expand. As the resultant expansion of M→S transformation is larger at higher spray currents (Fig. 4), presumably larger compressive stresses could contribute to the more pronounced crack healing observed in these coatings. Assuming a complete stress relaxation in the coatings after 20 h at 1300 °C, tensile thermal stresses would be still present in the coatings when they reach room temperature. Similar to the post-deposition thermal stresses, post-annealing thermal stresses can be anticipated to be larger at higher spray currents due to larger CTE mismatch stresses and high elastic modulus which could lead to larger crack openings at room temperature.

3.5 Sintering of amorphous Yb-silicate particles

In order to observe the viscous flow behavior of glassy Yb-silicate, sintering experiments were performed with plasma-sprayed particles as described in section 2.5. The cross-section images of the particles before and after 10 h heat treatments at various temperature steps (950 – 1300 °C) are shown in Fig. 7. From the comparison of Fig.7a and b, it can be seen that the original feedstock had a hollow spherical morphology (a) and after plasma spraying the melted and quenched particles were fully dense (b). It should be also mentioned that particles were almost fully amorphous after quenching according to XRD measurement. After 10 h of heat treatments at 950 and 1000 °C (Fig. 7 b1-b2), no changes were observed in particle morphologies while bonding between some of the particles started at 1025 °C as marked with arrows in Fig. 7 b3. After 10 h at 1050 °C (~crystallization temperature), the bonding degree of particles markedly increased (Fig. 7 b4) and the powder was not flowable anymore after this treatment (as well as after the following treatments). At higher temperatures (1100 and 1300 °C) a gradually reducing bonding between the particles after 10 h (Fig. 7 b5-b6) was observed suggesting that not only thermally activated diffusion based solid state sintering but also the viscous sintering was active.

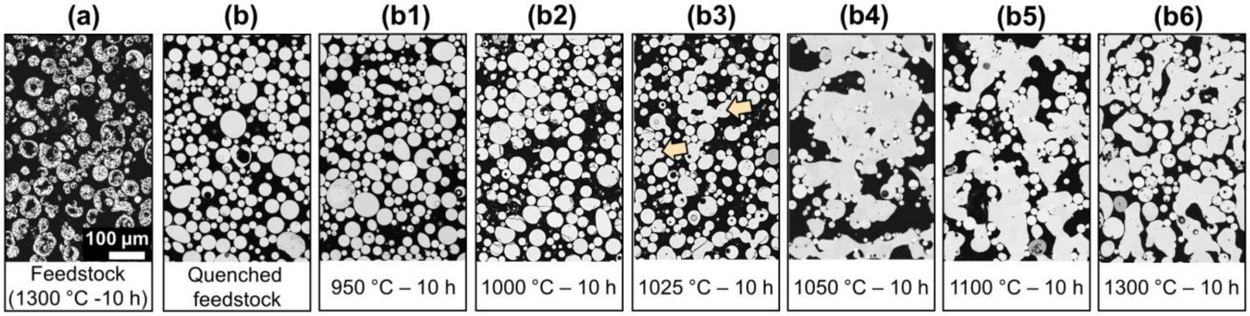

Figure 7: Cross-section SEM images of Yb-silicate particles; original feedstock after a heat treatment (1300 °C – 10 h) (a), plasma sprayed feedstock (b), plasma sprayed feedstock after 10 h heat treatments at various temperatures given below images (b1-b6). The arrows in b3 mark the neck formation between particles.

These results suggest that the glass transformation temperature of the quenched feedstock was right below the crystallization temperature (1000-1050 °C vs. 1050 °C) resulting in a drop in the viscosity and hence good bonding at 1050 °C. The temperature (T) dependence of glass viscosity (η) is described by the Vogel-Fulcher equation ($\eta = \eta_0 \, exp\,(C/(T - T_0))$), η_0 , C and T_0 are constants for the glass [54]) according to which the viscosity can decrease a few orders of magnitude with an increase in the temperature of 100 K. Therefore, the glass transition temperature was presumably already reached at 1025 °C but viscosity was not low enough to merge many adjacent particles as observed at 1050 °C. At higher temperatures (1100 and 1300 °C) on the other hand, the viscosity of the glass can be expected to be significantly reduced and accelerated the sintering process. However, as the crystallization temperature was exceeded at the same time, the viscosity increased possibly after a short time and stopped the viscous sintering process. Presumably, the crystallization kinetics were faster at the higher temperature (1300 °C vs. 1100 °C) and consequently, fewer particles could be bonded before the increase of viscosity (Fig. 7 b6 vs. b5).

3.6 Temperature-dependent heat treatments of APS Yb-silicate coatings

Bearing the sintering experiment results of the quenched powder in mind, a similar set of experiments was also conducted with APS Yb-silicate coating (on the substrate). The coating used in these experiments was sprayed at 325 A, but due to the switch to a new batch of $Yb_2Si_2O_7$ feedstock, some of the spray parameters were slightly altered to obtain a similar microstructure to the previous one. The experimental results including the results of crack area/width analyses and microstructure images of the coating both in the as-sprayed state and after 10 h heat treatments at different temperatures (b1-b6) are presented in Fig. 8. After 10 h heat treatment at 950 °C, there was no significant change in the crack area/width of the coating. At 1050 °C on the other hand all three stages of crack healing namely crack opening (i), crack spheroidization (ii), and crack closing (“healing”) (iii) were observed (Fig. 8 b3). Based on the powder sintering experiment results, this finding can be attributed to crystallization-hindered viscous flow at this temperature. Presumably, the initial aspect ratio of the crack is decisive in the stability of the crack, i.e. whether the crack transforms into a single sphere or breaks into two or more spheres as in a chain of spheres during the capillarity-induced healing process [55]. This could explain why some of the cracks were completely healed after 10 h, which is an assumption based on 2D SEM image, while some others were not. Apart from that, the viscosity level around the crack e.g. whether it is surrounded by amorphous or crystalline material should also affect the crack healing behavior for individual cracks according to the viscous flow hypothesis. As a result of the crack opening, which could be also affected by crystallization-induced shrinkage in the coating as mentioned above, and spheroidization, crack widths were approximately doubled at 1050 °C (Fig. 8a). The crack area did not change notably as the crack closure counteracted the area-increasing effect of crack opening and spheroidization. At higher temperatures (1100-1300 °C) both crack area and widths were reduced to a similar extent in comparison with the 1050 °C. At these high temperatures viscous flow and resulting particle sintering were less effective according to Fig. 7 b5-b6, therefore the contribution of other mechanisms such as metastable to stable phase transformation and solid state sintering to lower crack area and widths should be considered. Nevertheless, although the final crack area of the coating can be reduced after high-temperature heat treatments (> 1100 °C) with respect to the as-sprayed state, the final crack widths remained larger than that of the as-sprayed state (0.82 µm at 1300 °C vs. 0.64 µm). Based on the findings here, this result can be attributed to the incomplete crack healing process via viscous flow at 1050 °C due to the start of crystallization.

The bottom line is that the viscous flow would be desirable for the complete healing of cracks in the amorphous coatings if only it would not be stopped by the onset of crystallization. In the next section, therefore, whether the viscous flow in the coatings could be suppressed and based on that, whether or not the crack opening during the heat treatment could be prevented will be discussed.

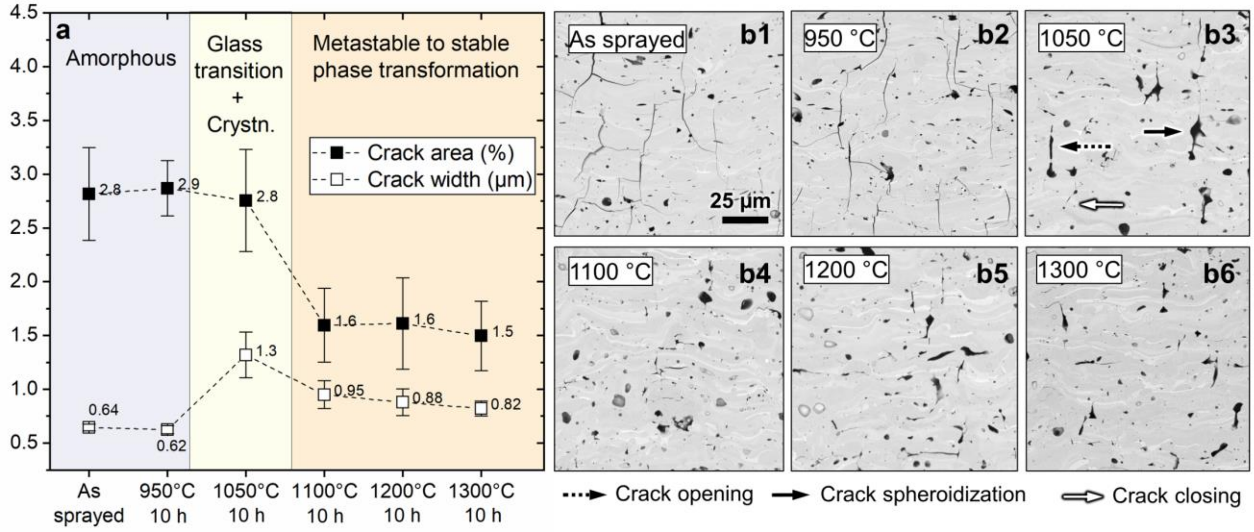

Figure 8: Crack area/width analyses results (a) and cross-section SEM microstructure images of Yb-silicate coating (325 A) in the as-sprayed state (b1) as well as after 10 h heat treatments at 950 (b2), 1050 (b3), 1100 (b4), 1200 (b5) and 1300 °C (b6). Data points in the graph show the mean values and error bars indicate the standard deviation (n=10).

3.7 Two-step heat treatment results

To suppress the viscous flow which started at 1025 °C according to powder sintering experiment results (Fig.7) and potentially avoid the resultant crack opening in the microstructure (Fig.8), two-step heat treatments were designed. Aiming to reduce the amorphous content by crystallization as well as the crack surface area, in other words, the driving force for the viscous flow when the glass transition temperature (1025 °C) is reached, the first step temperature of the heat treatment was selected to be 950, 975, and 1000 °C (<1025 °C). The dwell time at these temperatures also varied from 10 to 40 h. The higher degree of crystallinity of the coating after 10 h at 950 °C in comparison with the as-sprayed state can be seen in supplementary data as an example. The same trend of increasing crystallinity in the lower temperature region (<1025 °C) was also reported in our previous work even after shorter dwell time (~ 30 min) at the temperature [43]. The second step of the heat treatment was always 10 h at 1300 °C, which yielded the smallest average crack width according to Fig. 8a. The heating rate from room temperature to the first step as well as from the first to second step was 10 K/min. It should be noted that the heating rate possibly plays a critical role as it also affects the degree of crystallinity at a given temperature.

Fig. 9a shows the crack area, width, and total porosity analysis results of the coating after two-step heat treatments as well as in the as-sprayed state and after standard heat treatment (1300 °C-10 h) for comparison. Fig.9 b1-b4 presents the microstructure of the coating after two-step heat treatments. According to these results, the viscous flow could be suppressed below 1000 °C, given that crack area/width and total porosity could be slightly reduced up to this temperature in comparison with the as-sprayed state. At 1000 °C, crack widths were similar to that of standard heat treatment suggesting that the viscous flow was active. Increased temperature from 950 to 975 °C and prolonged dwell time from 20 to 40 h at 975 °C were beneficial to reduce the crack area and widths of the coating. This could be due to lower viscosity and surface energy at the glass transition temperature after these first step heat treatments due to increased crystallinity and crack healing via surface diffusion.

In contrast to standard heat treatment, two-step heat treatment (1^{st} step <1000 °C) reduced the total porosity and crack widths in the coating. Having said that, the crack area remained lower at the standard heat treatment (1.5% vs. 1.98% in the best case) suggesting viscous flow to be an effective crack healing mechanism at the expense of larger crack widths.

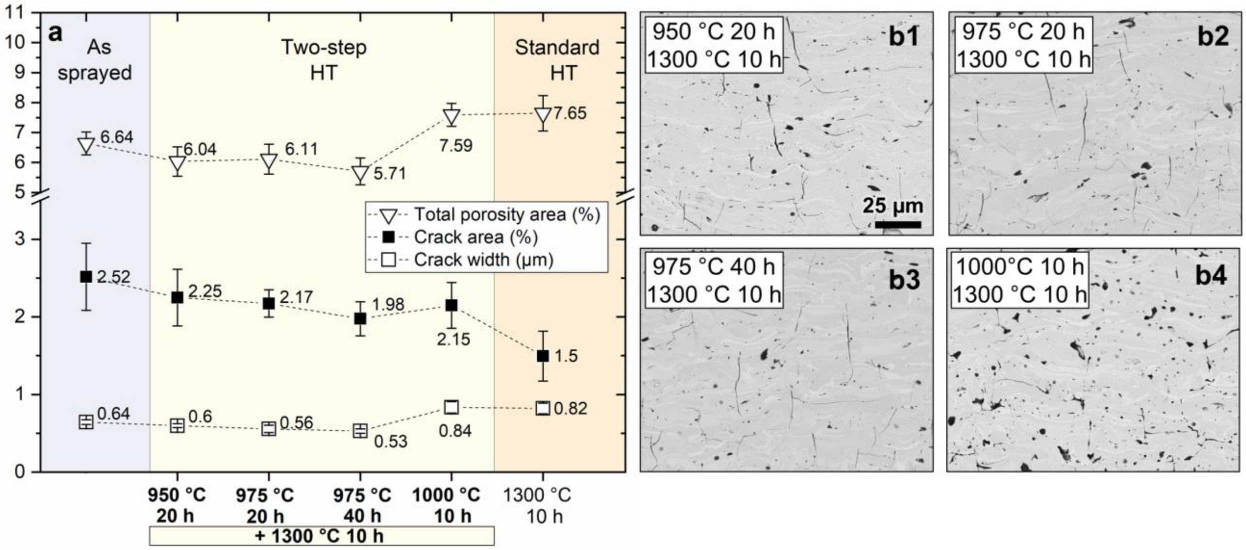

Figure 9: Crack area/width analyses results (a) and cross-section SEM microstructure images of Yb-silicate coating (325 A) after two-step heat treatments (b1-b4). The heat treatment conditions are indicated in each image. Data points in the graph show the mean values and error bars indicate the standard deviation (n=10).

4. Conclusions

Yb-silicate coatings were sprayed using the APS process under various deposition conditions which altered the amorphous content, degree of Si-evaporation, typical crack lengths and widths in the microstructure, and hence the total porosity in the coatings. The coatings were firstly subjected to a standard heat treatment (1300 °C-20 h) and the microstructural evolution was quantified in terms of crack area and widths.

Higher amorphous content in the coatings was correlated with the lower crack area after the heat treatment suggesting better crack healing. Crack widths were found to be larger after the heat treatment regardless of spray conditions. Changes in the crack area and widths were explained by the capillarity-driven viscous flow in the coatings. The viscous flow was found to be active above 1000 °C and experimentally shown to be resulting in crack healing (area reduction) and crack width enlargement (for the cracks which were not healed) in the coatings. Incomplete crack healing in the coatings was attributed to close onset temperatures of viscous flow (1000 °C) and crystallization (1050 °C) as the latter hinders the viscous flow by increasing viscosity. Based on these findings, a two-step heat treatment (e.g. 975 °C-20 h + 1300 °C-10 h) was tested aiming to suppress the viscous flow. By holding the coating below 1000 °C and presumably by reducing the amorphous content and surface energy before viscous flow starts, the viscous flow and hence resulting crack width enlargement could be prevented. Consequently, lower porosity was found in the coatings after the two-step heat treatments (1st step <1000 °C) in comparison with the as-sprayed state and standard heat treatment. The crack area however remained lowest after the standard heat treatment implying the effectiveness of viscous flow in crack healing at the expense of larger crack widths.

The prevailing questions are whether the cracks/porosity remain interconnected after the two-step heat treatment and how this compares to standard heat treatment. Because even if the total porosity is less and crack widths are smaller after the two-step heat treatment, better crack interconnectivity in comparison with the standard heat treatment may lead to higher permeation rates of the oxidants. These questions will be tackled in future research. In addition, further research will be required to elucidate the full set of mechanisms that drive the microstructural evolution of studied EBC systems.

Acknowledgments

The authors acknowledge the contributions of IEK-1 members, Karl-Heinz Rauwald, Ralf Laufs, and Frank Kurze for the APS experiments, Marie-Theres Gerhard for dilatometry measurements, and Volker Bader for performing the heat treatments.

References

[1] D.A. Lewis, M.T. Hogan, J. McMahon, K. S., Application of uncooled ceramic matrix composite power turbine blades for performance improvement of advanced turboshaft engines, Proceedings of the 64th American Helicopter Society International Annual Forum, Montreal, QC, Canada, 2008, pp. 961–966.

[2] A. Chamberlain , J. Lane, SiC/SiC ceramic matrix composites: A turbine engine perspective, in: W. Fahrenholtz, W.E. Lee, E.J. Wuchina, Y. Zhou (Eds.) Proceedings of Ultra-High Temperature Ceramics: Materials For Extreme Environmental Applications II, Hernstein, Austria, 2012.

[3] J. Lamon, N.P. Bansal, Ceramic Matrix Composites : Materials, Modeling and Technology, John Wiley & Sons, Incorporated, Somerset, UNITED STATES, 2014.

[4] E. Bakan, D.E. Mack, G. Mauer, R. Vaßen, J. Lamon, N.P. Padture, High-temperature materials for power generation in gas turbines, in: O. Guillon (Ed.), Advanced Ceramics for Energy Conversion and Storage, Elsevier Cambridge, MA,2020, pp. 3-62.

[5] E.J. Opila, J.L. Smialek, R.C. Robinson, D.S. Fox, N.S. Jacobson, SiC Recession Caused by SiO_2 Scale Volatility under Combustion Conditions: II, Thermodynamics and Gaseous-Diffusion Model, J. Am. Ceram. Soc. 82(7) (1999) 1826-1834.
[6] R.C. Robinson, J.L. Smialek, SiC Recession Caused by SiO_2 Scale Volatility under Combustion Conditions: I, Experimental Results and Empirical Model, J. Am. Ceram. Soc. 82(7) (1999) 1817-1825.
[7] H.E. Eaton, G.D. Linsey, K.L. More, J.B. Kimmel, J.R. Price, N. Miriyala, EBC Protection of SiC/SiC Composites in the Gas Turbine Combustion Environment, ASME Turbo Expo 2000: Power for Land, Sea, and Air, American Society of Mechanical Engineers, 2000, p. V004T02A018.
[8] K.N. Lee, R.A. Miller, N.S. Jacobson, Plasma sprayed mullite coatings on silicon-base ceramics, in: United States Patent (Ed.) 5,391,404, National Aeronautics and Space Administration, US, 1995.
[9] K.N. Lee, R.A. Miller, N.S. Jacobson, New Generation of Plasma-Sprayed Mullite Coatings on Silicon Carbide, J. Am. Ceram. Soc. 78(3) (1995) 705-710.
[10] K.N. Lee, Current status of environmental barrier coatings for Si-Based ceramics, Surf. Coat. Technol. 133–134 (2000) 1-7.
[11] H.E. Eaton, G.D. Linsey, E.Y. Sun, K.L. More, J.B. Kimmel, J.R. Price, N. Miriyala, EBC Protection of SiC/SiC Composites in the Gas Turbine Combustion Environment: Continuing Evaluation and Refurbishment Considerations, ASME Turbo Expo 2001: Power for Land, Sea, and Air, American Society of Mechanical Engineers, 2001, p. V004T02A010.
[12] K.N. Lee, D.S. Fox, J.I. Eldridge, D. Zhu, R.C. Robinson, N.P. Bansal, R.A. Miller, Upper Temperature Limit of Environmental Barrier Coatings Based on Mullite and BSAS, J. Am. Ceram. Soc. 86(8) (2003) 1299-1306.
[13] I. Spitsberg, J. Steibel, Thermal and Environmental Barrier Coatings for SiC/SiC CMCs in Aircraft Engine Applications*, International Journal of Applied Ceramic Technology 1(4) (2004) 291-301.
[14] K.N. Lee, D.S. Fox, N.P. Bansal, Rare earth silicate environmental barrier coatings for SiC/SiC composites and Si_3N_4 ceramics, J. Eur. Ceram. Soc. 25(10) (2005) 1705-1715.
[15] S. Ramasamy, S.N. Tewari, K.N. Lee, R.T. Bhatt, D.S. Fox, Slurry based multilayer environmental barrier coatings for silicon carbide and silicon nitride ceramics — I. Processing, Surf. Coat. Technol. 205(2) (2010) 258-265.
[16] Y. Wang, X. Chen, W. Liu, L. Cheng, L. Zhang, Exploration of YPO4 as a potential environmental barrier coating, Ceram. Int. 36(2) (2010) 755-759.
[17] J. Mesquita-Guimarães, E. García, P. Miranzo, M.I. Osendi, C.V. Cojocaru, R.S. Lima, Mullite–YSZ multilayered environmental barrier coatings tested in cycling conditions under water vapor atmosphere, Surf. Coat. Technol. 209 (2012) 103-109.
[18] C.V. Cojocaru, D. Lévesque, C. Moreau, R.S. Lima, Performance of thermally sprayed Si/mullite/BSAS environmental barrier coatings exposed to thermal cycling in water vapor environment, Surf. Coat. Technol. 216 (2013) 215-223.
[19] B.T. Richards, H.N.G. Wadley, Plasma spray deposition of tri-layer environmental barrier coatings, J. Eur. Ceram. Soc. 34(12) (2014) 3069-3083.
[20] K.N. Lee, Enviromental Barrier Coatings For SiC/SiC, in: N.P. Bansal, J. Lamon (Eds.) Ceramic Matrix Composites: Materials, Modeling and Technology, The American Ceramic Society, 2015.
[21] E. Bakan, D. Marcano, D. Zhou, Y.J. Sohn, G. Mauer, R. Vaßen, Yb2Si2O7 Environmental Barrier Coatings Deposited by Various Thermal Spray Techniques: A Preliminary Comparative Study, J. Therm. Spray Technol. 26(6) (2017) 1011-1024.
[22] K.N. Lee, Yb2Si2O7 Environmental barrier coatings with reduced bond coat oxidation rates via chemical modifications for long life, J. Am. Ceram. Soc. 102(3) (2019) 1507-1521.
[23] K.N. Lee, D.L. Waters, B.J. Puleo, A. Garg, W.D. Jennings, G. Costa, D.E. Sacksteder, Development of oxide-based High temperature environmental barrier coatings for ceramic matrix composites via the slurry process, J. Eur. Ceram. Soc. (2020).

[24] N. Rohbeck, P. Morrell, P. Xiao, Degradation of ytterbium disilicate environmental barrier coatings in high temperature steam atmosphere, J. Eur. Ceram. Soc. 39(10) (2019) 3153-3163.
[25] E. Garcia, H. Lee, S. Sampath, Phase and microstructure evolution in plasma sprayed Yb2Si2O7 coatings, J. Eur. Ceram. Soc. 39(4) (2019) 1477-1486.
[26] K.A. Kane, E. Garcia, R. Uwanyuze, M. Lance, K.A. Unocic, S. Sampath, B.A. Pint, Steam oxidation of ytterbium disilicate environmental barrier coatings with and without a silicon bond coat, J. Am. Ceram. Soc. 104(5) (2020) 2285-2300.
[27] E. Garcia, H.F. Garces, L.R. Turcer, H. Bale, N.P. Padture, S. Sampath, Crystallization behavior of air-plasma-sprayed ytterbium-silicate-based environmental barrier coatings, J. Eur. Ceram. Soc. 41(6) (2021) 3696-3705.
[28] R. Vaßen, E. Bakan, D. Sebold, Y.J. Sohn, Correlation of Process Conditions, Porosity Levels and Crystallinity in Atmospherically Plasma Sprayed Yb2Si2O7 Environmental Barrier Coatings, Journal of Composites Science 5(8) (2021) 198.
[29] D. Tejero-Martin, A.R. Romero, R.G. Wellman, T. Hussain, Interaction of CMAS on thermal sprayed ytterbium disilicate environmental barrier coatings: A story of porosity, Ceram. Int. 48(6) (2022) 8286-8296.
[30] H. Wang, J. Zhang, L. Sun, J. Wang, Microstructure and phase composition evolution of dual-phase ytterbium silicate coatings plasma sprayed from stoichiometric Yb2Si2O7 feedstock powder, Surf. Coat. Technol. (2022) 128373.
[31] E. Bakan, Y.J. Sohn, W. Kunz, H. Klemm, R. Vaßen, Effect of processing on high-velocity water vapor recession behavior of Yb-silicate environmental barrier coatings, J. Eur. Ceram. Soc. 39(4) (2019) 1507-1513.
[32] G. Mauer, R. Vaßen, D. Stöver, Preliminary study on the TriplexPro™-200 gun for atmospheric plasma spraying of yttria-stabilized zirconia, Surf. Coat. Technol. 202(18) (2008) 4374-4381.
[33] B.T. Richards, H. Zhao, H.N.G. Wadley, Structure, composition, and defect control during plasma spray deposition of ytterbium silicate coatings, Journal of Materials Science 50(24) (2015) 7939-7957.
[34] E. Bakan, G. Mauer, Y. Sohn, D. Koch, R. Vaßen, Application of High-Velocity Oxygen-Fuel (HVOF) Spraying to the Fabrication of Yb-Silicate Environmental Barrier Coatings, Coatings 7(4) (2017) 55.
[35] R. Vaßen, E. Bakan, C. Gatzen, S. Kim, D.E. Mack, O. Guillon, Environmental Barrier Coatings Made by Different Thermal Spray Technologies, Coatings 9(12) (2019) 784.
[36] S. Kuroda, T.W. Clyne, The quenching stress in thermally sprayed coatings, Thin Solid Films 200(1) (1991) 49-66.
[37] S. Kuroda, T. Dendo, S. Kitahara, Quenching stress in plasma sprayed coatings and its correlation with the deposit microstructure, J. Therm. Spray Technol. 4(1) (1995) 75-84.
[38] M. Mutter, G. Mauer, R. Mücke, O. Guillon, R. Vaßen, Correlation of splat morphologies with porosity and residual stress in plasma-sprayed YSZ coatings, Surf. Coat. Technol. 318 (2017) 157-169.
[39] H. Xiang, Z. Feng, Y. Zhou, Mechanical and thermal properties of Yb2SiO5: First-principles calculations and chemical bond theory investigations, J. Mater. Res. 29(15) (2014) 1609-1619.
[40] H.B. Guo, R. Vaßen, D. Stöver, Atmospheric plasma sprayed thick thermal barrier coatings with high segmentation crack density, Surf. Coat. Technol. 186(3) (2004) 353-363.
[41] T.A. Taylor, Thermal properties and microstructure of two thermal barrier coatings, Surf. Coat. Technol. 54 (1992) 53-57.
[42] S.V. Shinde, E.J. Gildersleeve V, C.A. Johnson, S. Sampath, Segmentation crack formation dynamics during air plasma spraying of zirconia, Acta Mater. 183 (2020) 196-206.
[43] E. Bakan, Y.J. Sohn, R. Vaßen, Metastable to stable phase transformation in atmospheric plasma sprayed Yb-silicate coating during post-heat treatment, Scripta Mater. 225 (2023) 115169.
[44] E.W. Washburn, The Dynamics of Capillary Flow, Physical Review 17(3) (1921) 273-283.
[45] J. Ilavsky, C.C. Berndt, J. Karthikeyan, Mercury intrusion porosimetry of plasma-sprayed ceramic, Journal of Materials Science 32(15) (1997) 3925-3932.

[46] R. Vaßen, X. Cao, F. Tietz, D. Basu, D. Stöver, Zirconates as New Materials for Thermal Barrier Coatings, J. Am. Ceram. Soc. 83(8) (2000) 2023-2028.
[47] E. Bakan, D.E. Mack, G. Mauer, R. Mücke, R. Vaßen, Porosity–Property Relationships of Plasma-Sprayed Gd2Zr2O7/YSZ Thermal Barrier Coatings, J. Am. Ceram. Soc. 98(8) (2015) 2647-2654.
[48] A. Guignard, G. Mauer, R. Vaßen, D. Stöver, Deposition and Characteristics of Submicrometer-Structured Thermal Barrier Coatings by Suspension Plasma Spraying, J. Therm. Spray Technol. 21(3) (2012) 416-424.
[49] P. Hrma, W.T. Han, A.R. Cooper, Thermal healing of cracks in glass, J. Non-Cryst. Solids 102(1) (1988) 88-94.
[50] R. Girard, A. Faivre, F. Despetis, Influence of Water on Crack Self-Healing in Soda-Lime Silicate Glass, J. Am. Ceram. Soc. 94(8) (2011) 2402-2407.
[51] S. Kanchika, F. Wakai, A model of crack healing of glass by viscous flow at elevated temperatures, J. Am. Ceram. Soc. 102(3) (2019) 1373-1378.
[52] M.N. Rahaman, Sintering of Ceramics, CRC Press 2007.
[53] A.R. Boccaccini, D.S. Brauer, L. Hupa, Bioactive Glasses: Fundamentals, Technology and Applications, Royal Society of Chemistry 2016.
[54] G.S. Fulcher, ANALYSIS OF RECENT MEASUREMENTS OF THE VISCOSITY OF GLASSES, J. Am. Ceram. Soc. 8(6) (1925) 339-355.
[55] F.A. Nichols, On the spheroidization of rod-shaped particles of finite length, Journal of Materials Science 11 (1976) 1077-1082.